



# Integrating plasmonic Au nanorods with dendritic like $\alpha$ -Bi<sub>2</sub>O<sub>3</sub>/Bi<sub>2</sub>O<sub>2</sub>CO<sub>3</sub> heterostructures for superior visible-light-driven photocatalysis

Changlin Yu <sup>a,\*</sup>, Wanqin Zhou <sup>a</sup>, Lihua Zhu <sup>a</sup>, Gao Li <sup>b</sup>, Kai Yang <sup>a,c</sup>, Rongchao Jin <sup>b,\*\*</sup>

<sup>a</sup> School of Metallurgy and Chemical Engineering, Jiangxi University of Science and Technology, 86 Hongqi Road, Ganzhou 341000, PR China

<sup>b</sup> Department of Chemistry, Carnegie Mellon University, Pittsburgh, PA 15213, United States

<sup>c</sup> State Key Laboratory of Photocatalysis on Energy and Environment, Fuzhou University, Fuzhou 350002, PR China



## ARTICLE INFO

### Article history:

Received 30 August 2015

Received in revised form 13 October 2015

Accepted 18 November 2015

Available online 25 November 2015

### Keywords:

$\alpha$ -Bi<sub>2</sub>O<sub>3</sub>/Bi<sub>2</sub>O<sub>2</sub>CO<sub>3</sub> heterostructure

Au nanospheres and nanorods

Surface plasmon resonance

Photocatalysis

Visible light

## ABSTRACT

To explore the relationship between semiconductor structure and plasmonic noble metal nanoparticles (NPs) property is crucial for developing highly efficient visible light driven photocatalyst. Here, dendritic  $\alpha$ -Bi<sub>2</sub>O<sub>3</sub>/Bi<sub>2</sub>O<sub>2</sub>CO<sub>3</sub> biphasic heterostructures were first synthesized by a facile and low-cost phase transformation method. Then, plasmonic Au NPs (including Au nanospheres (NSs, ~30 nm) and Au nanorods (NRs, ~20, ~30, and ~35 nm) were loaded onto the  $\alpha$ -Bi<sub>2</sub>O<sub>3</sub>/Bi<sub>2</sub>O<sub>2</sub>CO<sub>3</sub> heterostructure. The results revealed that these  $\alpha$ -Bi<sub>2</sub>O<sub>3</sub>/Bi<sub>2</sub>O<sub>2</sub>CO<sub>3</sub> heterostructures exhibited much higher visible-light photocatalytic activities than  $\alpha$ -Bi<sub>2</sub>O<sub>3</sub> for dye degradation. More importantly, compared to plain  $\alpha$ -Bi<sub>2</sub>O<sub>3</sub>/Bi<sub>2</sub>O<sub>2</sub>CO<sub>3</sub> heterostructures, loading of Au NSs brought ~4 times increase in activity and Au NRs 5–11 times depending on nanorods size. The significant boosting of activity is attributed to the large enhancement of charge separation by the formation of  $\alpha$ -Bi<sub>2</sub>O<sub>3</sub>/Bi<sub>2</sub>O<sub>2</sub>CO<sub>3</sub> interface and more production of  $\cdot$ OH radicals by Au NSs or Au NRs. The surface plasmon resonance (SPR) absorption of these gold NPs on the  $\alpha$ -Bi<sub>2</sub>O<sub>3</sub>/Bi<sub>2</sub>O<sub>2</sub>CO<sub>3</sub> heterostructures could also have significant contribution to the activities due to their strong plasmonic near-fields. This work demonstrates that tailoring the semiconductor substrate structure and the plasmonic noble metal NPs properties should constitute a promising strategy for the design efficient solar energy driven photocatalytic materials.

© 2015 Elsevier B.V. All rights reserved.

## 1. Introduction

Photocatalysis is an environmentally friendly and promising technology in environmental purification and converting solar energy into chemical energy [1–10]. Noble metal elements play an important role in enhancing photocatalytic performance. For example, noble metal oxides or sulphides (RuO<sub>2</sub> [11], IrO<sub>2</sub> [12], PdS [13]) can act as cocatalyst [14] to exert distinct synergistic effect in enhancing photocatalytic activity for water splitting. Of particular interest is the application of noble metal nanoparticles (NPs) to reduce the photo-generated e<sup>−</sup>/h<sup>+</sup> recombination rate and thus enhance photocatalytic activity. This is owing to the better charge separation, i.e., the photo-generated electrons readily accumulate

on the metal component, while holes remain on the photocatalyst surface [15–17].

More recently, noble metal NPs plasmon-induced photocatalysis has been gaining significant attention due to its high throughput and low excitation-energy requirements [18,19]. The major drawback of the widely used TiO<sub>2</sub> photocatalyst is its large band gap (~3.2 eV) which limits its optical absorption within the UV light region (2–4% of the entire solar spectrum). However, in plasmon-induced photocatalysis, noble metal NPs (e.g., Au, Ag) can absorb visible light via surface plasmon resonance (SPR). The plasmon-excited electrons in the noble metal NPs can be transferred to the conduction band of adjacent semiconductor [20,21] and the photo-generated charge carriers are thus efficiently separated, giving rise to enhanced photocatalytic activity [22]. Moreover, it was found that SPR can create intense local electromagnetic fields which in turn enhance sub-bandgap absorption in TiO<sub>2</sub> and thus increase the photocatalytic activity in the visible range [23]. The desirable plasmonic properties of noble metal NPs have promoted the con-

\* Corresponding author.

\*\* Corresponding author.

E-mail addresses: [yuchanglinjx@163.com](mailto:yuchanglinjx@163.com) (C. Yu), [rongchao@andrew.cmu.edu](mailto:rongchao@andrew.cmu.edu) (R. Jin).

cept of assembling plasmonic noble metal NPs together with certain semiconductors that can offer relatively high surface area as well as active sites to produce visible light responsive composite photocatalysts. In these composite materials, noble metal NPs and the substrates work in a cooperative way to enhance the photocatalytic activity.

At present, gold (Au) NPs have been attracting much attention because they can strongly interact with light in the visible and near-infrared region due to their extraordinary SPR properties and also because of their remarkable photostability [24–34]. The plasmon-induced photocatalytic performance of Au is strongly related to the properties of Au NPs (particle size, morphology, etc.) and substrates (semiconductor type, crystal phase, crystallinity, morphology, etc.) and the interactions between Au NPs and substrates. For example, Subramanian et al. [35] investigated the size-dependent catalytic activity of Au NPs in the  $\text{TiO}_2/\text{Au}$  composite and found that the size-dependent shift in the apparent Fermi level of the  $\text{TiO}_2$ –Au composite (20 mV for 8 nm diameter, 40 mV for 5 nm and 60 mV for 3 nm Au NPs) shows the ability of Au NPs to influence the energetics by improving the photoinduced charge separation. She et al. [36] reported that Janus Au– $\text{TiO}_2$  nanostructures with large Au NPs (50 nm) showed highly efficient visible-light hydrogen generation due to their strong localization of plasmonic near-fields close to the Au– $\text{TiO}_2$  interface. Moreover, Liu et al. [37] found that depositing Au NPs onto  $\text{TiO}_2$  nanoflakes showed high efficiency and ultrastability for the degradation of the azo dye brilliant red X-3B, and the ultrafine metal particle size and strong metal-support interaction were considered as the key factors for the overall photocatalytic activity. With respect to the influence of substrate crystal phase, the photocatalytic production of  $\text{H}_2$  over  $\text{Au}/\text{TiO}_2$  anatase was found to be around two orders of magnitude higher than that recorded for  $\text{Au}/\text{TiO}_2$  rutile [38]. More interestingly, Tsukamoto et al. [39] observed that Au particles located at the interface of anatase/rutile  $\text{TiO}_2$  particles could behave as the active sites for aerobic photocatalytic oxidation via plasmon activation of the Au particles by visible light followed by consecutive electron transfer in the Au/rutile/anatase contact sites. Formation of interface or heterojunction between two semiconductors is an effective strategy in enhancing the separation of photogenerated electron–hole pairs [40]. For example, the formation of phase junction between the surfaces of anatase and rutile NPs could greatly enhance the photocatalytic activity for  $\text{H}_2$  production [41]. The above results indicate that design and fabrication of Au NPs/semiconductor heterostructures hold promise as an effective strategy to develop highly efficient visible-light-driven photocatalysts.

In this work, dendritic  $\alpha\text{-Bi}_2\text{O}_3/\text{Bi}_2\text{O}_2\text{CO}_3$  heterostructures are first successfully prepared via a phase transformation method. Then, large plasmonic Au NPs prepared by wet chemistry methods, including Au nanospheres (NSs,  $30 \pm 3$  nm) and single crystal Au nanorods (NRs,  $20 \pm 4$ ,  $30 \pm 5$ , and  $35 \pm 4$  nm) were loaded onto  $\alpha\text{-Bi}_2\text{O}_3/\text{Bi}_2\text{O}_2\text{CO}_3$  heterostructures. The as-prepared Au/ $\alpha\text{-Bi}_2\text{O}_3/\text{Bi}_2\text{O}_2\text{CO}_3$  hybrid nanostructures possess interesting optical properties and highly efficient photocatalytic performance in degradation of dye under visible light irradiation. In comparison to the previously reported Au plasmonic photocatalysts, our Au/ $\alpha\text{-Bi}_2\text{O}_3/\text{Bi}_2\text{O}_2\text{CO}_3$  hybrid nanostructures are superior in three aspects for plasmon-enhanced photocatalytic reactions: (1) the substrate is a unique  $\alpha\text{-Bi}_2\text{O}_3/\text{Bi}_2\text{O}_2\text{CO}_3$  heterostructure prepared by a facile, low-cost and one-step method. (2) Au NPs have uniform size and morphology, which benefits the understanding of the effect of Au NPs property on plasmon-enhanced performance. (3) Intimate integration of plasmonic NPs and the light-harvesting semiconductors could be effective in improving the photocatalytic performance, offering the potential of studying a wide variety of plasmonic photocatalysts with heterostructures.

## 2. Experimental

### 2.1. Preparation of catalysts

#### 2.1.1. Synthesis of dendritic like $\alpha\text{-Bi}_2\text{O}_3/\text{Bi}_2\text{O}_2\text{CO}_3$ heterostructure

All chemicals were purchased from Sigma–Aldrich. 5 mmol  $\text{Bi}(\text{NO}_3)_3 \cdot 5\text{H}_2\text{O}$  was dissolved in a dilute (1 M)  $\text{HNO}_3$  solution, and then 3.75 mmol sodium citrate ( $\text{Na}_3\text{C}_6\text{H}_5\text{O}_7$ ) was added to the above solution. The mixture was stirred for ~10 min until a clear solution was formed. Finally, the pH value of the solution was adjusted to 4 using 2.0 M NaOH under stirring. The formed white-colored precursor was transferred into a Teflon-lined stainless steel autoclave and heated to 180 °C and maintained at this temperature (total time 24 h). The gray product was isolated by centrifugation, washed with distilled water and absolute ethanol for several times, then dried in vacuum at 90 °C for 5 h to give rise to  $\text{Bi}_2\text{O}_2\text{CO}_3$  nanosquares. In air atmosphere, the as-prepared  $\text{Bi}_2\text{O}_2\text{CO}_3$  was placed a muffle furnace at 350 °C and calcined for 10 or 20 min, then taken out immediately, which gave rise to biphasic  $\alpha\text{-Bi}_2\text{O}_3/\text{Bi}_2\text{O}_2\text{CO}_3$  heterostructures.

#### 2.1.2. Synthesis of Au nanospheres (NSs) (~30 nm) and nanorods (NRs) (~20 nm, ~30 nm, ~35 nm)

This method is similar to our previous report [42]. In this procedure, there are two primary steps. The first step is to prepare Au seeds. 364 mg cetyltrimethylammonium bromide (CTAB) and 1 mg  $\text{HAuCl}_4 \cdot 3\text{H}_2\text{O}$  was dissolved in 10 mL nanopure water in a tri-neck 25 mL round bottom flask. After 10 min, 0.6 mL (10 mM)  $\text{NaBH}_4$  was added to the flask under vigorous magnetic stirring. The as-obtained Au seeds were used in the growth of nanorods. The second step is to prepare Au nanorods. 364 mg CTAB, 2 mg  $\text{HAuCl}_4 \cdot 3\text{H}_2\text{O}$  and different amounts of 4 mM  $\text{AgNO}_3$  solution (10  $\mu\text{L}$ , 20  $\mu\text{L}$ , 50  $\mu\text{L}$ , 100  $\mu\text{L}$ ) were mixed in 10 mL nanopure water in a tri-neck 25 mL round bottom flask. After stirring 10 min, 70  $\mu\text{L}$  (78.8 mM) ascorbic acid was added to the flask. The flask was immersed in a warm water bath at 27–30 °C, and 12  $\mu\text{L}$  of Au seed was added and the reaction was allowed to proceed for 1 h. Finally, the excess CTAB was separated by centrifugation and one obtained Au NSs and NRs with different sizes.

#### 2.1.3. Synthesis of Au loaded $\alpha\text{-Bi}_2\text{O}_3/\text{Bi}_2\text{O}_2\text{CO}_3$ heterostructure

Au nanocrystals were loaded onto  $\alpha\text{-Bi}_2\text{O}_3/\text{Bi}_2\text{O}_2\text{CO}_3$  by the impregnation method. Typically, 100 mg  $\alpha\text{-Bi}_2\text{O}_3/\text{Bi}_2\text{O}_2\text{CO}_3$  powders were impregnated by a Au NPs solution. After stirring for 24 h at room temperature, Au loaded  $\alpha\text{-Bi}_2\text{O}_3/\text{Bi}_2\text{O}_2\text{CO}_3$  powders were collected by centrifugation and dried at 120 °C in a vacuum oven. The final mass content of Au over  $\alpha\text{-Bi}_2\text{O}_3/\text{Bi}_2\text{O}_2\text{CO}_3$  is 0.85–0.90% determined by XPS ESCALAB 250. No silver was detected.

### 2.2. Characterization of catalysts

The thermogravimetric analysis (TGA) was performed with Seiko instruments TGA/SDTA 6300 at a heating rate of 10 °C  $\text{min}^{-1}$  from room temperature to 700 °C under air flow. Powder X-ray diffraction data were recorded on a X’Pert PRO X-ray diffractometer at 40 kV and 40 mA for monochromatized  $\text{Cu K}\alpha$  ( $\lambda = 1.5418 \text{ \AA}$ ) radiation. The morphology of the samples was analyzed by scanning electron microscopy (SEM) on a LEO 1450VP scanning electron microscope. Transmission electron microscopy (TEM) image was recorded on a Tecnai 20 FEG microscope. The valence states of elements were analyzed by XPS using a thermo scientific ESCALAB 250 system with a monochromatic  $\text{Al K}\alpha$  source and a charge neutralizer. The UV–vis diffuse reflectance spectra were recorded on a UV–vis spectrophotometer (UV-2550, Shimadzu). The absorption spectra were referenced to  $\text{BaSO}_4$ . The

nitrogen adsorption–desorption isotherm was measured using a Micromeritics ASAP 2020 physisorption analyzer. The photocurrent measurement was carried out by using a standard three-electrode system with the help of CHI660D electrochemical workstation. Graphite electrode, standard calomel electrode and the as-prepared samples played a role of counter electrode, reference electrode, and working electrode, respectively. The electrolyte solution was 0.1 mol/L sodium sulfate solution. 0.01 g catalyst was dispersed into 0.4 mL 0.05 wt% Nafion ethanol solution with sonication for 30 min, then 20  $\mu$ L slurry was dropped on fluorine-tin oxide (FTO) glass substrates to make working electrode. The light source was simulative solar light (Xenon lamp, perfect light PLS-SXE300, Beijing). The light intensity is about 100  $\mu$ w/cm<sup>2</sup>.

### 2.3. Catalytic performance

The photocatalytic performance of the prepared samples was evaluated by measuring the degradation of methyl orange under visible light irradiation. The light source is the same as literature [8]. A 150 W quartz halogen lamp (Dolan Jenner Fiber-Lite MI-150 Illuminator) with a cutoff filter solution jacket (HCl aqueous solution of  $\text{CuSO}_4$  (0.5 M) and  $\text{K}_2\text{CrO}_4$  (0.002 M)), which cuts off wavelengths shorter than 400 nm and longer than 660 nm was used as the light source. The distance from the light source to reaction solution is around 10 cm. The light intensity is around 70  $\mu$ w/cm<sup>2</sup>. 0.05 g photocatalyst was suspended in 100 mL aqueous solution of methyl orange with the concentration of  $C_0 = 0.020$  g/L. Prior to light illumination, the suspension was magnetically stirred for 40 min in the dark for attaining adsorption/desorption equilibrium. The suspension was vigorously stirred during the photocatalytic reaction process. The reaction mixture was sampled at given time intervals during light illumination. After centrifugation, the dye or phenol concentration was measured on a UV-vis spectrophotometer (Agilent, HP8453). The method of active species trapping experiment is the same as photoactivity tests.

### 2.4. Radicals trapping

In photoactivity tests for  $\cdot\text{OH}$  generation, coumarin (10 mM in a 10 mM  $\text{FeCl}_3$  solution) was used as a chemical trap of  $\cdot\text{OH}$  radicals because coumarin readily reacts with  $\cdot\text{OH}$  to form a highly fluorescent product, 7-hydroxycoumarin (7HC). The experimental procedure was similar to the measurement of photocatalytic activity. The fluorescence emission intensity of 7-hydroxycoumarin was measured at 460 nm under the excitation at 332 nm using a Fluorolog spectrofluorometer (HORIBA, Jobin Yvon) after centrifugation.

## 3. Results and discussions

### 3.1. Catalyst characterization

#### 3.1.1. TG

The  $\alpha\text{-Bi}_2\text{O}_3$ / $\text{Bi}_2\text{O}_2\text{CO}_3$  heterostructures were prepared by a calcination method via the partial phase transformation of  $\text{Bi}_2\text{O}_2\text{CO}_3$ .  $\text{Bi}_2\text{O}_2\text{CO}_3$  nanosquares were first synthesized under hydrothermal conditions. TGA measurements were carried out to determine the temperature for phase transformation of  $\text{Bi}_2\text{O}_2\text{CO}_3$  during the temperature increase. Fig. 1(a) shows that there are two weight loss steps. The first weight loss of 1.46%, from 216 to 300 °C, could be caused by dehydration. From 297 to 390 °C,  $\text{Bi}_2\text{O}_2\text{CO}_3$  phase began to transform to  $\alpha\text{-Bi}_2\text{O}_3$ , which caused the second weight loss of 8.26%, corresponding to the transformation reaction:  $\text{Bi}_2\text{O}_2\text{CO}_3 \rightarrow \alpha\text{-Bi}_2\text{O}_3 + \text{CO}_2$ ,  $\Delta m = -9.4\%$  (referenced to  $\text{Bi}_2\text{O}_2\text{CO}_3$ ).

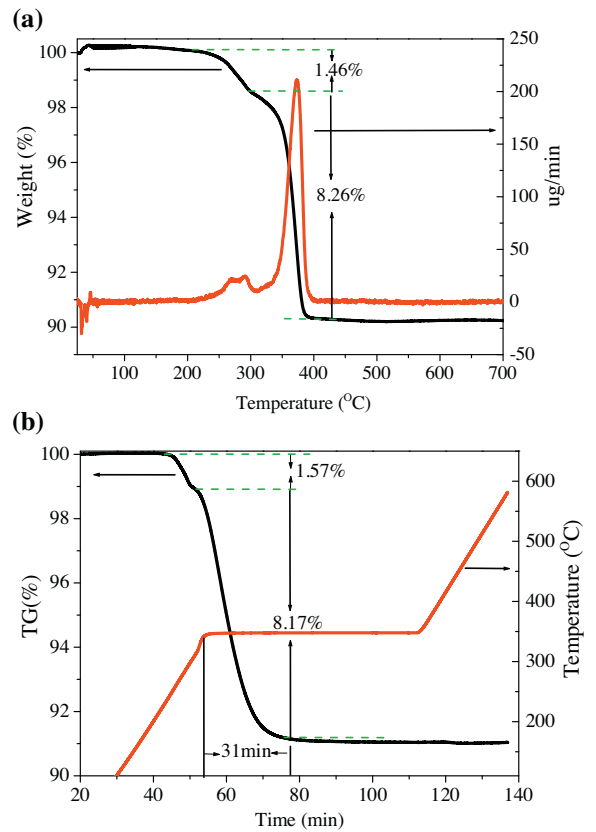


Fig. 1. TGA profiles of  $\text{Bi}_2\text{O}_2\text{CO}_3$  powders in air. (a) Weight loss vs temperature; (b) weight loss vs time.

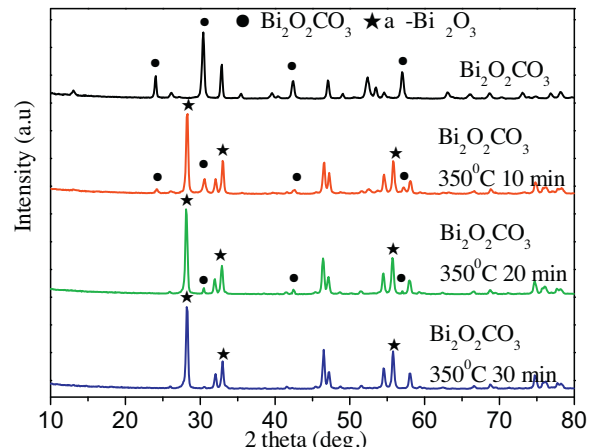


Fig. 2. XRD patterns of the initial  $\text{Bi}_2\text{O}_2\text{CO}_3$  and samples after calcination at 350 °C for different times (10 min, 20 min, 30 min).

Fig. 1(b) suggests that by maintaining the temperature at 350 °C, the duration for transformation from  $\text{Bi}_2\text{O}_2\text{CO}_3$  to  $\alpha\text{-Bi}_2\text{O}_3$  is ~31 min.

#### 3.1.2. XRD

The above data indicates that by precise control of the calcination time and temperature, biphasic  $\alpha\text{-Bi}_2\text{O}_3$ / $\text{Bi}_2\text{O}_2\text{CO}_3$  heterostructures could be obtained. Thus, 0.2 g of the initially prepared  $\text{Bi}_2\text{O}_2\text{CO}_3$  nanosquares was placed in a furnace at 350 °C and calcined for different times (10, 20, 30 min). Fig. 2 shows the XRD patterns of the as-prepared samples. The initial  $\text{Bi}_2\text{O}_2\text{CO}_3$  (prior to calcination) shows sharp and intense diffraction peaks, which can all be indexed as a tetragonal phase of  $\text{Bi}_2\text{O}_2\text{CO}_3$  (JCPDS card

No. 41-1488,  $a = 3.865 \text{ \AA}$ ,  $b = 3.865 \text{ \AA}$ ,  $c = 13.675 \text{ \AA}$ ). No peaks from impurities such as  $(\text{BiO})_4\text{CO}_3(\text{OH})_2$  are detected in XRD pattern [43,44]. When  $\text{Bi}_2\text{O}_2\text{CO}_3$  was calcined at  $350^\circ\text{C}$  for 10 min, new reflection peaks at  $2\theta$  of 28.29, 33.01, and  $55.79^\circ$  appear. These new reflection peaks are ascribed to the tetragonal phase of  $\alpha\text{-Bi}_2\text{O}_3$  with the lattice constants of  $a = b = 7.740 \text{ \AA}$  and  $c = 5.632 \text{ \AA}$ , which are consistent with the values from the standard JCPDS card No. 71-2274. After heat treatment at  $350^\circ\text{C}$  for 30 min, the characteristic diffraction peaks of  $\text{Bi}_2\text{O}_2\text{CO}_3$  are completely disappeared. Obviously,  $\text{Bi}_2\text{O}_2\text{CO}_3$  calcined at  $350^\circ\text{C}$  for 10 or 20 min shows the distinct diffraction peaks of both  $\text{Bi}_2\text{O}_2\text{CO}_3$  and  $\alpha\text{-Bi}_2\text{O}_3$  phases, indicating the formation of  $\alpha\text{-Bi}_2\text{O}_3/\text{Bi}_2\text{O}_2\text{CO}_3$  composite phases.

### 3.1.3. SEM and TEM

**Fig. 3** shows the SEM images of the initial  $\text{Bi}_2\text{O}_2\text{CO}_3$  and samples calcined at  $350^\circ\text{C}$  for different times. The initial  $\text{Bi}_2\text{O}_2\text{CO}_3$  is composed of predominant plates with different sizes. When heated at  $350^\circ\text{C}$  for 10 min, these plates aggregated together and the plate-like morphology disappeared gradually with heating time. When the calcination time was increased to 20 or 30 min, the aggregated plates were transformed to linked rod-like particles with length of 0.2–0.5  $\mu\text{m}$ . The detail morphology was further analyzed by TEM.

The TEM image in **Fig. 4(a)** indicates that the  $\text{Bi}_2\text{O}_2\text{CO}_3$  particles show nanosquare morphology with length of  $\sim 100 \text{ nm}$  and width of  $\sim 50 \text{ nm}$ . **Fig. 4(b)–(d)** indicates that when calcined at  $350^\circ\text{C}$ , the dispersed nanosquares were fused together, forming dendritic particles. The morphology change was caused by the transformation of  $\text{Bi}_2\text{O}_2\text{CO}_3 \rightarrow \alpha\text{-Bi}_2\text{O}_3/\text{Bi}_2\text{O}_2\text{CO}_3 \rightarrow \alpha\text{-Bi}_2\text{O}_3$ . These results show that the unique dendritic  $\alpha\text{-Bi}_2\text{O}_3/\text{Bi}_2\text{O}_2\text{CO}_3$  nanoheterostructures can be obtained via calcination of  $\text{Bi}_2\text{O}_2\text{CO}_3$ . Thermal decomposition reaction of  $\text{Bi}_2\text{O}_2\text{CO}_3$  could be a complex kinetic process. **Fig. 5** illustrates the characteristic and formation mechanism of the produced dendritic like  $\alpha\text{-Bi}_2\text{O}_3/\text{Bi}_2\text{O}_2\text{CO}_3$  nanoheterostructures.  $\text{Bi}_2\text{O}_2\text{CO}_3$  is thermally unstable and when heating temperature is over  $350^\circ\text{C}$ , partial decomposition of  $\text{Bi}_2\text{O}_2\text{CO}_3$  to  $\alpha\text{-Bi}_2\text{O}_3$  occurs. The formation of  $\alpha\text{-Bi}_2\text{O}_3$  is a solid reaction process. The grain size of the reactant substrate decreases gradually due to the transition of  $\text{Bi}_2\text{O}_2\text{CO}_3$ , as detected by TEM. The as-produced grain boundary is a reactive site for thermal decomposition. Because of the reaction at the grain boundary, the respective grains of the internal  $\text{Bi}_2\text{O}_2\text{CO}_3$  are coated by  $\alpha\text{-Bi}_2\text{O}_3$ . Therefore, in the limited calcination time,  $\text{Bi}_2\text{O}_2\text{CO}_3$  particles could be coated by a surface product layer of  $\alpha\text{-Bi}_2\text{O}_3$  and formed  $\alpha\text{-Bi}_2\text{O}_3/\text{Bi}_2\text{O}_2\text{CO}_3$  heterostructure with well contacted interface. The formation of a surface  $\alpha\text{-Bi}_2\text{O}_3$  layer over  $\text{Bi}_2\text{O}_2\text{CO}_3$  at the beginning of thermal decomposition could cause the later slow reaction by blocking the diffusion of  $\text{CO}_2$ . At the same time, the surface morphology of  $\alpha\text{-Bi}_2\text{O}_3$  crystal depends on the extent of deviation of the formation conditions from the thermodynamic equilibrium or the driving force for crystallization. Specifically, dendrites will form when the formation conditions are far from the thermodynamic equilibrium because of the increasing contribution of mass diffusion [45,46]. In other words, when the  $\alpha\text{-Bi}_2\text{O}_3$  growth rate is larger than that of the mass transport of ions that feed the growing crystals, the dendrite growth will be promoted. The formation of a surface  $\alpha\text{-Bi}_2\text{O}_3$  layer over  $\text{Bi}_2\text{O}_2\text{CO}_3$  could block the diffusion of  $\text{CO}_2$  and hinder the mass transport, which could contribute to thermodynamic unequilibrium state of  $\alpha\text{-Bi}_2\text{O}_3$  growth. The as-produced  $\alpha\text{-Bi}_2\text{O}_3$  particles are fused together and finally produce dendritic like  $\alpha\text{-Bi}_2\text{O}_3/\text{Bi}_2\text{O}_2\text{CO}_3$  nanostructure. The color changes sequentially from gray  $\rightarrow$  shallow yellow  $\rightarrow$  deep yellow over the phase transformations.

Au nanospheres (NSs) and Au nanorods (NRs) with different size were prepared by a wet chemistry method [42]. **Fig. 6** shows the photograph of the prepared Au NPs aqueous solutions (colloids).

The prepared Au NSs ( $\sim 30 \text{ nm}$ ) and Au NRs ( $\sim 20 \text{ nm}$ ) colloids show the brilliant ruby-red color. Au NRs colloids ( $\sim 30 \text{ nm}$  and  $\sim 35 \text{ nm}$ ) exhibit the deep red color. The difference in color was caused by the different optical properties (e.g., absorption and scattering) of Au colloids, which were determined by the shape and size of Au NPs [47].

**Fig. 7** shows the TEM images of the Au NPs. **Fig. 7(a)** shows the Au NPs with diameter of  $30 \pm 3 \text{ nm}$ . **Fig. 7(b)–(d)** shows the Au NRs with different length and diameter. **Fig. 7(b)** shows Au NRs of  $20 \pm 4 \text{ nm}$  in length and  $15 \pm 1 \text{ nm}$  diameter. **Fig. 7(c)** shows Au NRs of  $15 \pm 2 \text{ nm}$  diameter and length of  $30 \pm 5 \text{ nm}$ . **Fig. 7(d)** shows Au NRs of  $13 \pm 1 \text{ nm}$  diameter and length of  $35 \pm 4 \text{ nm}$ . According to previous research [42], these Au NRs are fcc crystalline with  $[1\ 1\ 0]$  as the growth direction (i.e., the long axis). The structural model for the nanorod is shown in **Fig. 7(e)**, in which the side faces consist of four  $\{1\ 1\ 1\}$  facets and two  $\{1\ 0\ 0\}$  facets; note that the two  $\{1\ 0\ 0\}$  facets are formed due to longitudinal truncation of the  $\{1\ 1\ 1\}$  (otherwise, the four  $\{1\ 1\ 1\}$  planes form a parallel-agonal radial cross section of the rod); this truncation is better observed from the end view of the rod. The typical high resolution (HRTEM) TEM image of Au NRs ( $30 \text{ nm}$ )/ $\alpha\text{-Bi}_2\text{O}_3/\text{Bi}_2\text{O}_2\text{CO}_3$  sample is shown in **Fig. 7(f)**. As observed in the HRTEM image, a single crystalline Au NR is deposited over the surface of the crystalline  $\alpha\text{-Bi}_2\text{O}_3$ . The measured lattice spacing of the crystalline substrate  $\alpha\text{-Bi}_2\text{O}_3$  ( $d = 0.33 \text{ nm}$ ) corresponds to the  $(1\ 2\ 0)$  spacing of  $\alpha\text{-Bi}_2\text{O}_3$  phase [48]. Some particles with no obvious lattice spacing could be the undecomposed  $\text{Bi}_2\text{O}_2\text{CO}_3$  particles. The single-crystalline Au nanorod shows lattice fringe of  $0.203 \text{ nm}$ , matching the crystallographic planes of metallic cubic-phase Au ( $2\ 0\ 0$ ). The HRTEM result suggests that the Au/ $\alpha\text{-Bi}_2\text{O}_3/\text{Bi}_2\text{O}_2\text{CO}_3$  sample manifests as the heterostructures with well contacted interfaces.

### 3.1.4. SEM and TEM

**Fig. 8(a)** shows the UV-vis spectra of the Au colloids. It can be seen that the shape and structural anisotropy of Au NPs substantially influence their SPR absorption. Au NSs show a distinct peak at  $530 \text{ nm}$  due to the SPR extinction [49]. The three Au NR colloids display different SPR peaks. Au NRs ( $\sim 20 \text{ nm}$ ) give rise to the peak at  $532 \text{ nm}$ , and the longitudinal SPR peak of Au NRs ( $\sim 30 \text{ nm}$ ) shifts to  $608 \text{ nm}$  and a shoulder peak (i.e., traverse SPR) at around  $530 \text{ nm}$  was also observed. The Au NRs ( $\sim 35 \text{ nm}$ ) show the major SPR peak at  $697 \text{ nm}$  and a shoulder peak at  $\sim 515 \text{ nm}$ . The change in the major peak wavelength is mainly due to the variation in the anisotropy of Au NRs (aspect ratio). Here, the aspect ratio is defined as the ratio of the nanorod length to its diameter. The values of aspect ratio of Au NRs ( $\sim 20 \text{ nm}$ ), Au NRs ( $\sim 30 \text{ nm}$ ) and Au NRs ( $\sim 35 \text{ nm}$ ) are estimated to be 1.3, 2.0, and 3.5, respectively. The increase in structural anisotropy shifts the SPR to the longer wavelength direction.

**Fig. 8(b)** shows the UV-vis diffuse reflectance spectra of the as-prepared  $\text{Bi}_2\text{O}_2\text{CO}_3$  and  $\text{Bi}_2\text{O}_2\text{CO}_3$  calcined at  $350^\circ\text{C}$  for different times. The absorption edge of  $\text{Bi}_2\text{O}_2\text{CO}_3$  is estimated to be at  $370 \text{ nm}$  (**Fig. 8b**). The calcination treatment makes the absorption edges shift from  $370 \text{ nm}$  to  $537$ ,  $545$ , and  $548 \text{ nm}$ , corresponding to  $\text{Bi}_2\text{O}_2\text{CO}_3$  calcined at  $350^\circ\text{C}$  for 10, 20, and 30 min, respectively. The produced  $\alpha\text{-Bi}_2\text{O}_3/\text{Bi}_2\text{O}_2\text{CO}_3$  heterostructures and  $\alpha\text{-Bi}_2\text{O}_3$  exhibit intense absorption in the visible light region. The band gap energies of the produced samples were estimated from the intercept of the tangents to the plots of  $(\alpha h\nu)^{1/2}$  vs photon energy [50] (see Supplementary data Fig. S1(a)–(b)). The estimated band gap energies were approximately  $3.18 \text{ eV}$  for  $\text{Bi}_2\text{O}_2\text{CO}_3$ ,  $2.17 \text{ eV}$  for  $\alpha\text{-Bi}_2\text{O}_3/\text{Bi}_2\text{O}_2\text{CO}_3$  ( $220^\circ\text{C}$ , 10 min),  $2.08 \text{ eV}$  for  $\alpha\text{-Bi}_2\text{O}_3/\text{Bi}_2\text{O}_2\text{CO}_3$  ( $220^\circ\text{C}$ , 20 min), and  $2.12 \text{ eV}$  for  $\alpha\text{-Bi}_2\text{O}_3$ .

**Fig. 8(c)** shows the UV-vis diffuse reflectance spectra of the Au loaded  $\alpha\text{-Bi}_2\text{O}_3/\text{Bi}_2\text{O}_2\text{CO}_3$  ( $220^\circ\text{C}$ , 20 min) composites. Integrating plasmonic Au NSs ( $\sim 30 \text{ nm}$ ) or NRs ( $\sim 20 \text{ nm}$ ) onto  $\alpha\text{-Bi}_2\text{O}_3/\text{Bi}_2\text{O}_2\text{CO}_3$  slightly increases its absorption in the visible light

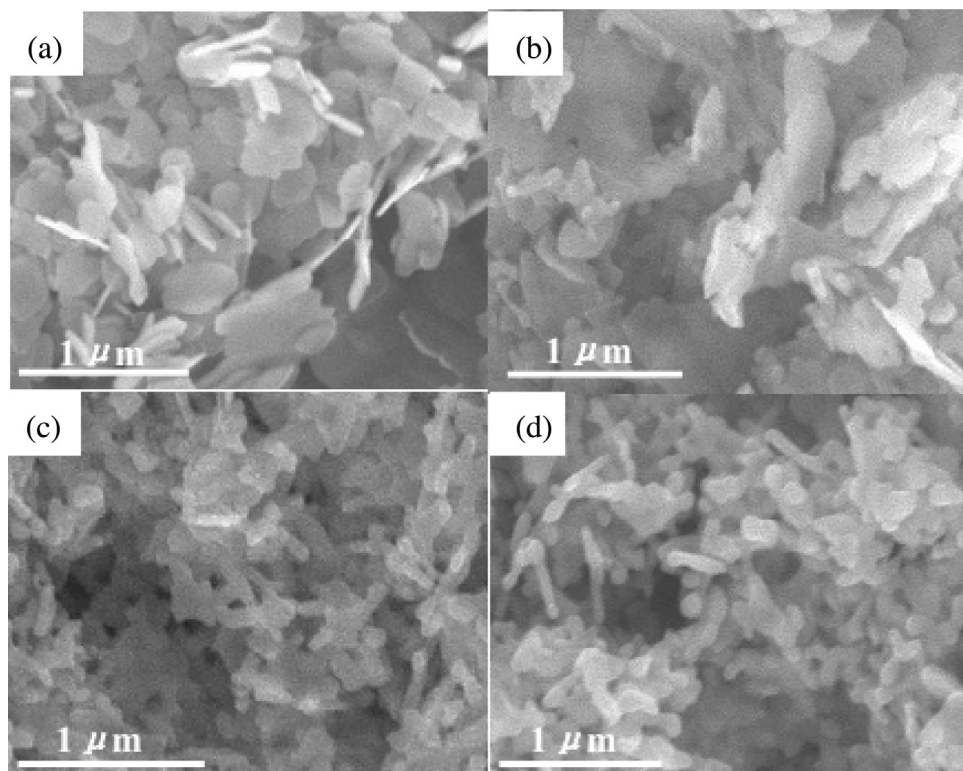


**Fig. 3.** SEM images of the samples. (a)  $\text{Bi}_2\text{O}_2\text{CO}_3$ ; (b)–(d) for  $\text{Bi}_2\text{O}_2\text{CO}_3$  samples calcined at  $350^\circ\text{C}$  for 10 min, 20 min, and 30 min, respectively.

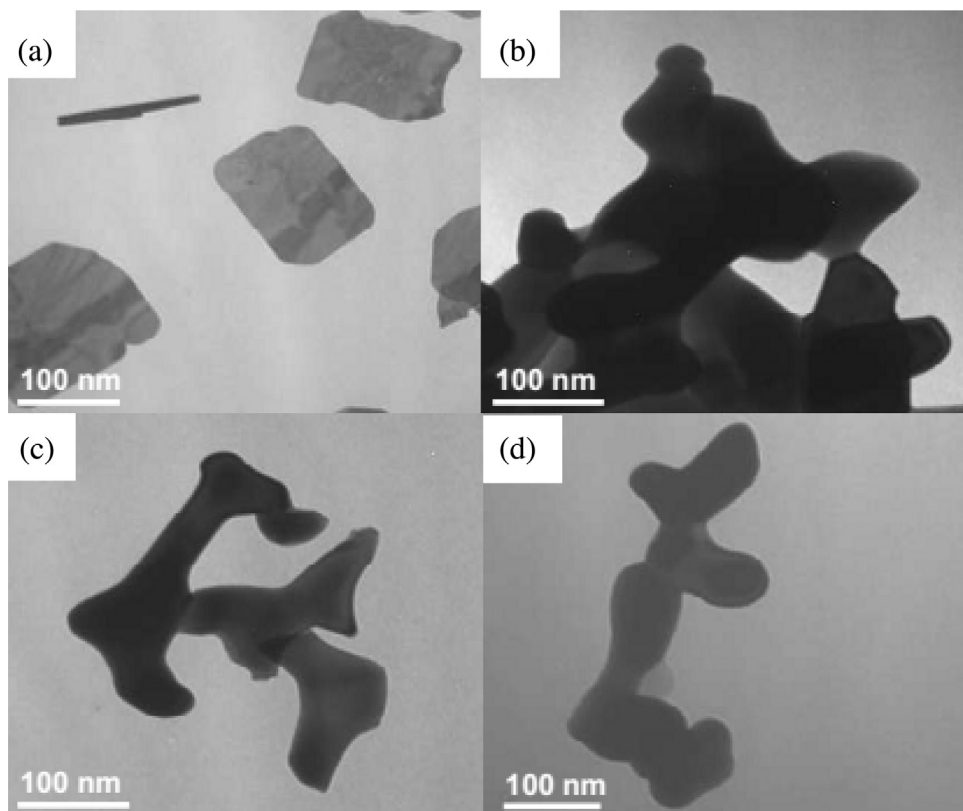


**Fig. 4.** TEM images of the samples. (a)  $\text{Bi}_2\text{O}_2\text{CO}_3$ ; (b)–(d) for  $\text{Bi}_2\text{O}_2\text{CO}_3$  samples calcined at  $350^\circ\text{C}$  for 10 min, 20 min, and 30 min, respectively.

region. However, no obvious plasmonic resonance peaks of Au NSs (530 nm) and NRs ( $\sim 20$  nm) (532 nm) was detected, which should be caused by the  $\sim 530$  nm SPR band of Au NPs being shorter than

the bandgap ( $2.1\text{ eV} = 590\text{ nm}$ ) of the  $\alpha\text{-Bi}_2\text{O}_3/\text{Bi}_2\text{O}_2\text{CO}_3$  substrate. When Au NRs ( $\sim 30$  nm) were loaded on  $\alpha\text{-Bi}_2\text{O}_3/\text{Bi}_2\text{O}_2\text{CO}_3$ , an obvious absorption band at  $\sim 606$  nm appeared. This absorption

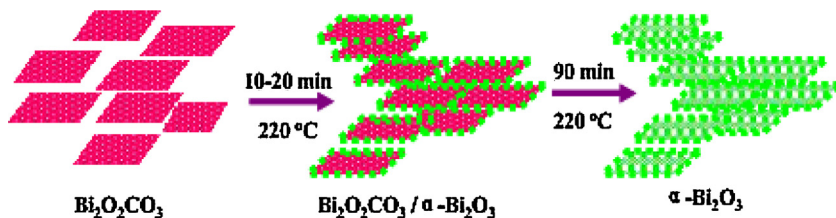


**Fig. 5.** Schematic model of the formation dendritic  $\alpha\text{-Bi}_2\text{O}_3/\text{Bi}_2\text{O}_2\text{CO}_3$  heterostructure during the course of  $\text{Bi}_2\text{O}_2\text{CO}_3$  calcination in air atmosphere.



**Fig. 6.** Photographs of the prepared Au NSs ( $\sim 30$  nm) and Au NRs with different size ( $\sim 20$ ,  $\sim 30$  and  $\sim 35$  nm) aqueous solutions. The concentration of Au NPs is  $0.5 \text{ m M}^{-1}$ . Nanospheres: NSs, Au nanorods: NRs.

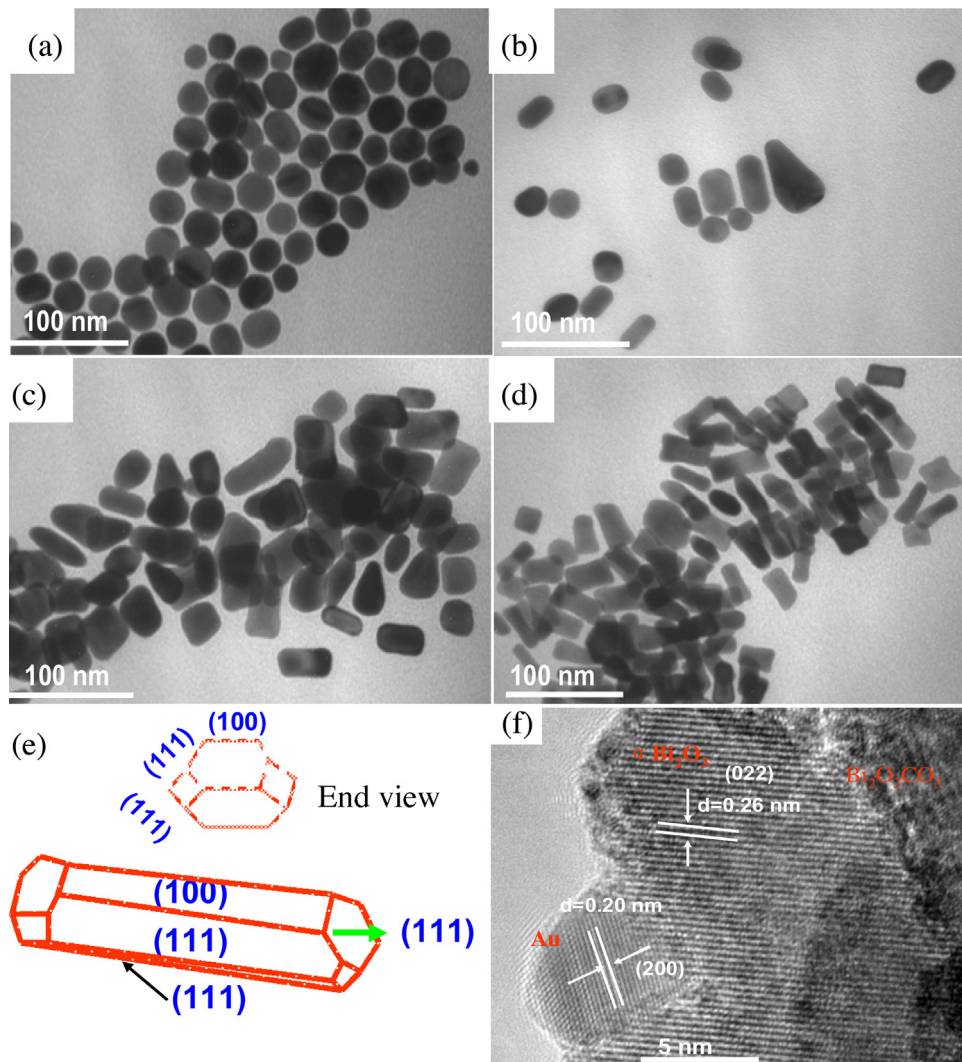


**Fig. 7.** (a) TEM images of the Au NSs ( $\sim 30$  nm), (b)–(d) Au NRs with different sizes ( $\sim 20$ ,  $\sim 30$  and  $\sim 35$  nm), (e) structural model of single crystalline Au nanorods, (f) high resolution TEM image of Au NRs ( $\sim 30$  nm)/ $\alpha\text{-Bi}_2\text{O}_3/\text{Bi}_2\text{O}_2\text{CO}_3$ . Nanospheres: NSs, Au nanorods: NRs.

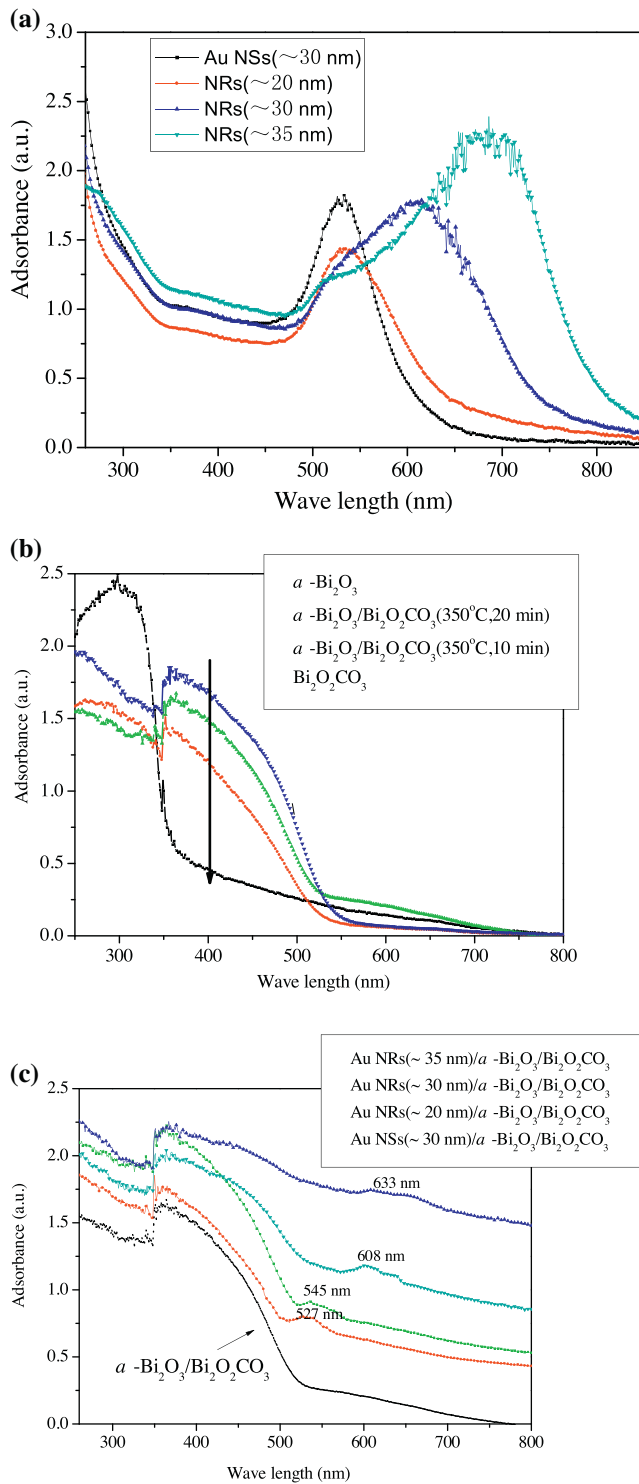


**Fig. 8.** (a) UV-vis spectra of the prepared Au colloids; (b) UV-vis diffuse reflectance spectra of Bi<sub>2</sub>O<sub>3</sub> and Bi<sub>2</sub>O<sub>3</sub> samples calcined at 350 °C for 10 min, 20 min, and 30 min; (c) UV-vis diffuse reflectance spectra of the Au/α-Bi<sub>2</sub>O<sub>3</sub>-Bi<sub>2</sub>O<sub>2</sub>CO<sub>3</sub> (NRs: nanorods, NSs: nanospheres).

band was ascribed to the SPR of Au NRs since this peak is similar to that of Au NRs (~30 nm) colloids. A similar absorption band from 600 to 670 nm was observed after loading Au NRs (~35 nm). This result indicates that integrating plasmonic Au NRs with  $\alpha$ -Bi<sub>2</sub>O<sub>3</sub>/Bi<sub>2</sub>O<sub>2</sub>CO<sub>3</sub> heterostructure could substantially increase the visible light absorption by the hybrid material.

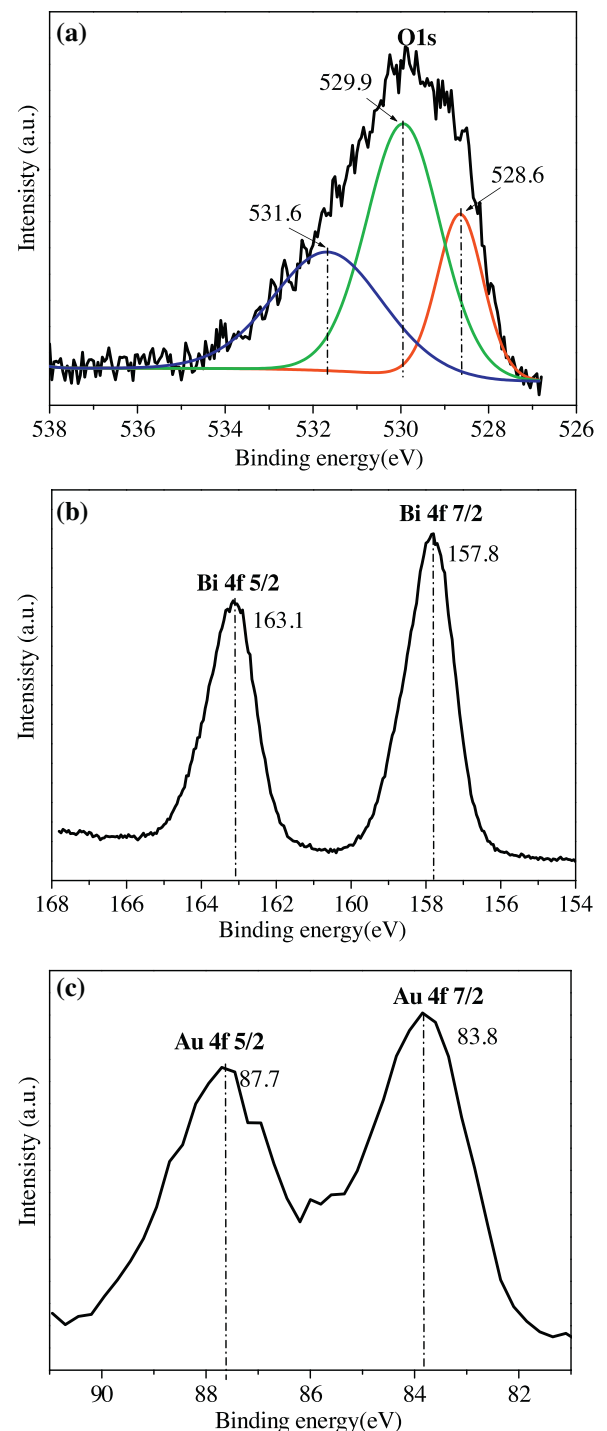


**Fig. 9.** High resolution XPS spectra of O1s, Bi 4f and Au 4f of the Au NRs (~30 nm)/ $\alpha$ -Bi<sub>2</sub>O<sub>3</sub>/Bi<sub>2</sub>O<sub>2</sub>CO<sub>3</sub>.

### 3.1.5. XPS

XPS was used to investigate the valence state of elements in Au NRs (~30 nm) supported on  $\alpha$ -Bi<sub>2</sub>O<sub>3</sub>-Bi<sub>2</sub>O<sub>2</sub>CO<sub>3</sub>. Fig. 9(a) shows the high resolution XPS spectrum of O1s. Obviously, the O1s region can be deconvoluted into three peaks at 531.6, 529.9 and 528.6 eV, indicating the co-existence of three distinguishable chemical states of oxygen on this surface. The peak at 529.9 eV is ascribed to the oxygen attached to the Bi-O bond [51] and the peak around 531.1 eV can be assigned to carbonate species [50]. The affiliation of the peak at 528.6 eV is not clear because the characteristic peak of adsorbed H<sub>2</sub>O (or surface hydroxyl groups) is 532.2 eV [42,50]. Fig. 9(b) shows

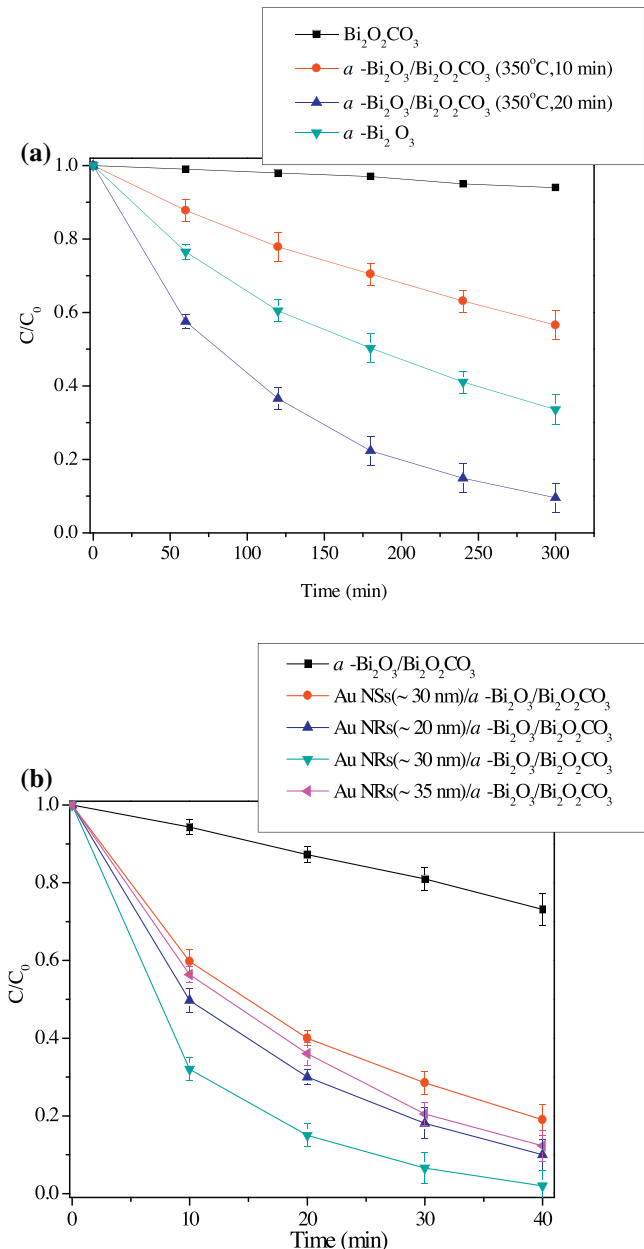


**Fig. 10.** Photocatalytic activity comparison of the prepared samples in degradation of methyl orange. (a) Performance of  $\text{Bi}_2\text{O}_2\text{CO}_3$  and  $\text{Bi}_2\text{O}_2\text{CO}_3$  samples calcined at  $350^\circ\text{C}$  for 10, 20, and 30 min, respectively; the effects of loading Au NSs and Au NRs with different size on photocatalytic activity. Nanospheres: NSs, nanorods: NRs.

the high-resolution XPS spectrum of Bi 4f. The Bi 4f spectrum can be deconvoluted into two peaks. The binding energy of 163.1 eV is for the Bi 4f<sub>5/2</sub> and 157.8 eV for Bi 4f<sub>7/2</sub>. The dominant chemical state of Bi in the sample is +3 [52]. In Fig. 9(c), the binding energies of Au 4f<sub>5/2</sub> and Au 4f<sub>7/2</sub> are at 87.7 and 83.8 eV, respectively, which are attributed to metallic Au [53].

### 3.2. Catalytic performances

The photocatalytic activities of the as-prepared samples were evaluated by photodegradation of dye, methyl orange (MO), under visible light irradiation. As shown in Fig. 10(a),  $\text{Bi}_2\text{O}_2\text{CO}_3$  exhibited almost no photocatalytic activity in the MO degradation reaction due to its poor visible light absorption. Among them,  $\alpha\text{-Bi}_2\text{O}_3/\text{Bi}_2\text{O}_2\text{CO}_3$  heterostructure prepared by calcination of

**Table 1**

Textural properties, band gap of the materials, and photocatalysis rate constants in degradation of MO.

| Material   | $S$ ( $\text{m}^2/\text{g}$ ) <sup>a</sup> | $E_g$ (eV) <sup>b</sup> | $k$ ( $\text{min}^{-1}$ ) <sup>c</sup> |
|--|--|-------------------------|--|
| $\text{Bi}_2\text{O}_2\text{CO}_3$   | 6.3  | 3.18                    | 0                                      |
| $\alpha\text{-Bi}_2\text{O}_3/\text{Bi}_2\text{O}_2\text{CO}_3$ (350 °C, 10 min)                             | 4.4  | 2.17                    | 0.0019                                 |
| $\alpha\text{-Bi}_2\text{O}_3/\text{Bi}_2\text{O}_2\text{CO}_3$ (350 °C, 20 min)                             | 3.8  | 2.08                    | 0.0078                                 |
| $\alpha\text{-Bi}_2\text{O}_3$   | 3.2  | 2.12                    | 0.0036                                 |
| Au NSs ( $\sim 30\text{ nm}$ )- $\alpha\text{-Bi}_2\text{O}_3/\text{Bi}_2\text{O}_2\text{CO}_3$ <sup>d</sup> | 3.5  | –                       | 0.0410                                 |
| Au NRs ( $\sim 20\text{ nm}$ )- $\alpha\text{-Bi}_2\text{O}_3/\text{Bi}_2\text{O}_2\text{CO}_3$ <sup>d</sup> | 3.2  | –                       | 0.0562                                 |
| Au NRs ( $\sim 30\text{ nm}$ )- $\alpha\text{-Bi}_2\text{O}_3/\text{Bi}_2\text{O}_2\text{CO}_3$ <sup>d</sup> | 3.4  | –                       | 0.0940                                 |
| Au NRs ( $\sim 35\text{ nm}$ )- $\alpha\text{-Bi}_2\text{O}_3/\text{Bi}_2\text{O}_2\text{CO}_3$ <sup>d</sup> | 3.1  | –                       | 0.0520                                 |

<sup>a</sup> BET surface area.

<sup>b</sup> Band gap.

<sup>c</sup> The pseudo-first-order rate constant in degradation of MO and phenol, respectively.

<sup>d</sup>  $\alpha\text{-Bi}_2\text{O}_3/\text{Bi}_2\text{O}_2\text{CO}_3$  was obtained by calcination of  $\text{Bi}_2\text{O}_2\text{CO}_3$  at  $350^\circ\text{C}$  for 20 min. NSs: nanospheres, NRs: nanorods.

$\text{Bi}_2\text{O}_2\text{CO}_3$  at  $350^\circ\text{C}$  for 20 min exhibited the highest photocatalytic activity. The pseudo-first-order rate constants (see Table 1 and Supplementary data Fig. S2) for  $\alpha\text{-Bi}_2\text{O}_3/\text{Bi}_2\text{O}_2\text{CO}_3$  ( $350^\circ\text{C}$ , 10 min),  $\alpha\text{-Bi}_2\text{O}_3/\text{Bi}_2\text{O}_2\text{CO}_3$  ( $350^\circ\text{C}$ , 20 min) and  $\alpha\text{-Bi}_2\text{O}_3$  are 0.0019, 0.0078 and  $0.0036\text{ min}^{-1}$ , respectively. Although the surface area of the three samples is similar, the photocatalytic decomposition rate of MO over the  $\alpha\text{-Bi}_2\text{O}_3/\text{Bi}_2\text{O}_2\text{CO}_3$  ( $350^\circ\text{C}$ , 20 min) is 4.1 times the activity of  $\alpha\text{-Bi}_2\text{O}_3/\text{Bi}_2\text{O}_2\text{CO}_3$  ( $350^\circ\text{C}$ , 10 min), and 2.1 times that of  $\alpha\text{-Bi}_2\text{O}_3$ , respectively.

The effects of integrating plasmonic Au NSs or NRs with  $\alpha\text{-Bi}_2\text{O}_3/\text{Bi}_2\text{O}_2\text{CO}_3$  ( $350^\circ\text{C}$ , 20 min) on the photocatalytic activity are shown in Fig. 10(b). Notably, loading Au NSs or NRs on  $\alpha\text{-Bi}_2\text{O}_3/\text{Bi}_2\text{O}_2\text{CO}_3$  heterostructures could further substantially increase the photocatalytic efficiency. MO dye was completely degraded in 40 min over Au NRs ( $\sim 30\text{ nm}$ )- $\alpha\text{-Bi}_2\text{O}_3/\text{Bi}_2\text{O}_2\text{CO}_3$  under visible light irradiation, whereas the degradation rate of MO over  $\alpha\text{-Bi}_2\text{O}_3/\text{Bi}_2\text{O}_2\text{CO}_3$  was only  $\sim 27\%$  at the same light irradiation time. The degradation rate constant ( $0.0940\text{ min}^{-1}$ ) over Au NRs ( $\sim 30\text{ nm}$ )- $\alpha\text{-Bi}_2\text{O}_3/\text{Bi}_2\text{O}_2\text{CO}_3$  is 12 times that over  $\alpha\text{-Bi}_2\text{O}_3/\text{Bi}_2\text{O}_2\text{CO}_3$  ( $0.0078\text{ min}^{-1}$ ). Moreover, we found that Au NRs exhibit more distinct effects on promoting activity than Au NSs. To test the stability of the best composite photocatalyst (Au NRs ( $\sim 30\text{ nm}$ )- $\alpha\text{-Bi}_2\text{O}_3/\text{Bi}_2\text{O}_2\text{CO}_3$ ), we carried out the recycle test. The obtained results are shown in Table S1. From Table S1, we can see that the activity of the composite photocatalyst only shows a slight decrease with the increase of recycling times, which indicates that the composite photocatalyst has good stability. The SEM and TEM images of the composite photocatalyst after cycling three times are shown in Fig. S3(a) and (b). From Fig. S3(a) and (b), we can see that compared with the fresh photocatalyst, the morphology of the reacted photocatalyst did not appear obvious variation.

### 3.3. Discussion

To understand the role of Au NPs and the electron transport paths in the efficient photocatalysis of the  $\text{Au}/\alpha\text{-Bi}_2\text{O}_3/\text{Bi}_2\text{O}_2\text{CO}_3$  heterostructured catalyst, we first calculated the electronic band structures of  $\alpha\text{-Bi}_2\text{O}_3/\text{Bi}_2\text{O}_2\text{CO}_3$  (see Supplementary data for details), then the generation of the hydroxyl radicals ( $\bullet\text{OH}$ ) in the visible light irradiated suspensions of the photocatalysts was studied [54]. The top of the valence band (VB) and the bottom of the conduction band (CB) of  $\text{Bi}_2\text{O}_2\text{CO}_3$  are calculated to be 3.56 and  $0.276\text{ eV}$ , respectively. Accordingly, the VB and CB of  $\alpha\text{-Bi}_2\text{O}_3$  are estimated to be 2.33 and  $0.11\text{ eV}$ , respectively. The Supplementary data Fig. S3 shows the detail electronic band structure of  $\alpha\text{-Bi}_2\text{O}_3/\text{Bi}_2\text{O}_2\text{CO}_3$ . Therefore, on the  $\alpha\text{-Bi}_2\text{O}_3/\text{Bi}_2\text{O}_2\text{CO}_3$  heterostructure, the CB level of  $\alpha\text{-Bi}_2\text{O}_3$  ( $0.11\text{ eV}$ ) is slightly more negative than that of  $\text{Bi}_2\text{O}_2\text{CO}_3$  ( $0.28\text{ eV}$ ). Under visible

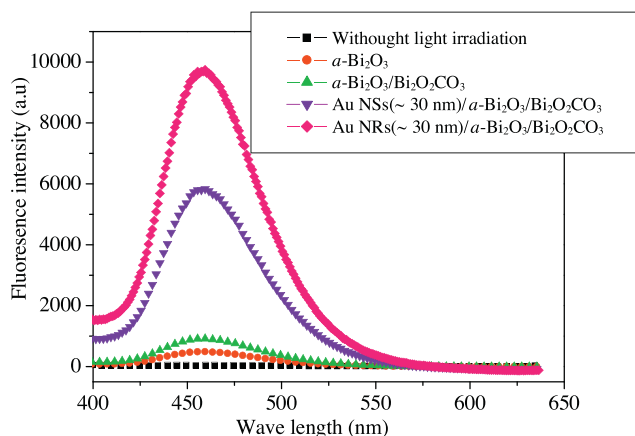


**Fig. 11.** Fluorescence emission intensities of the coumarin-OH adduct (7-hydroxycoumarin) produced in the suspensions of  $\alpha$ -Bi<sub>2</sub>O<sub>3</sub>,  $\alpha$ -Bi<sub>2</sub>O<sub>3</sub>/Bi<sub>2</sub>O<sub>2</sub>CO<sub>3</sub>, Au NSs (~30 nm)/ $\alpha$ -Bi<sub>2</sub>O<sub>3</sub>/Bi<sub>2</sub>O<sub>2</sub>CO<sub>3</sub> and AuNRs (~30 nm)/ $\alpha$ -Bi<sub>2</sub>O<sub>3</sub>/Bi<sub>2</sub>O<sub>2</sub>CO<sub>3</sub> after the visible light irradiation for 40 min. Nanospheres: NSs, nanorods: NRs.

light irradiation, the excited electrons in  $\alpha$ -Bi<sub>2</sub>O<sub>3</sub> could transfer to the VB of Bi<sub>2</sub>O<sub>2</sub>CO<sub>3</sub>, which promotes the separation of the electron and hole pairs photogenerated on the  $\alpha$ -Bi<sub>2</sub>O<sub>3</sub>. The generation of •OH radicals on the photo-illuminated  $\alpha$ -Bi<sub>2</sub>O<sub>3</sub>,  $\alpha$ -Bi<sub>2</sub>O<sub>3</sub>/Bi<sub>2</sub>O<sub>2</sub>CO<sub>3</sub>, Au NSs (~30 nm)/ $\alpha$ -Bi<sub>2</sub>O<sub>3</sub>/Bi<sub>2</sub>O<sub>2</sub>CO<sub>3</sub> and NRs (~30 nm)/ $\alpha$ -Bi<sub>2</sub>O<sub>3</sub>/Bi<sub>2</sub>O<sub>2</sub>CO<sub>3</sub> in the presence of Fe<sup>3+</sup> was detected by a fluorescence technique using coumarin as a chemical trap of •OH radicals [54,55]. Coumarin readily reacts with •OH to form a highly fluorescent product, 7-hydroxycoumarin. **Fig. 11** dis-

plays the fluorescence emission intensities of the coumarin •OH adduct (7-hydroxycoumarin) produced in suspensions of the four samples after the visible light irradiation for 40 min. It can be clearly observed that the intensity followed the order:  $\alpha$ -Bi<sub>2</sub>O<sub>3</sub> <  $\alpha$ -Bi<sub>2</sub>O<sub>3</sub>/Bi<sub>2</sub>O<sub>2</sub>CO<sub>3</sub> < Au NSs (~30 nm)/ $\alpha$ -Bi<sub>2</sub>O<sub>3</sub>/Bi<sub>2</sub>O<sub>2</sub>CO<sub>3</sub> < Au NRs (~30 nm)/ $\alpha$ -Bi<sub>2</sub>O<sub>3</sub>/Bi<sub>2</sub>O<sub>2</sub>CO<sub>3</sub>, which indicates that the produced •OH radical concentration could follow the same order. More •OH radicals were generated by Au NRs (~30 nm)/ $\alpha$ -Bi<sub>2</sub>O<sub>3</sub>/Bi<sub>2</sub>O<sub>2</sub>CO<sub>3</sub> under the same photocatalytic condition. The detected •OH radicals are produced directly through the reaction of H<sub>2</sub>O with the hole generated on the valence band of the photo-excited  $\alpha$ -Bi<sub>2</sub>O<sub>3</sub>. The formation of  $\alpha$ -Bi<sub>2</sub>O<sub>3</sub>/Bi<sub>2</sub>O<sub>2</sub>CO<sub>3</sub> heterostructure and loading of Au NPs on  $\alpha$ -Bi<sub>2</sub>O<sub>3</sub> favor the production of more •OH, which reveals an efficient separation of the electron and hole pairs in the photo-excited  $\alpha$ -Bi<sub>2</sub>O<sub>3</sub>/Bi<sub>2</sub>O<sub>2</sub>CO<sub>3</sub> and Au/ $\alpha$ -Bi<sub>2</sub>O<sub>3</sub>/Bi<sub>2</sub>O<sub>2</sub>CO<sub>3</sub> systems.

To further demonstrate the influence of heterostructur and AuNRs on the separation efficiency on photogenerated electrons and holes, we carried out the photocurrent test. The obtained results of the typical samples (Bi<sub>2</sub>O<sub>2</sub>CO<sub>3</sub> (b)  $\alpha$ -Bi<sub>2</sub>O<sub>3</sub>/Bi<sub>2</sub>O<sub>2</sub>CO<sub>3</sub>,  $\alpha$ -Bi<sub>2</sub>O<sub>3</sub>, Au NRs (~30 nm)- $\alpha$ -Bi<sub>2</sub>O<sub>3</sub>/Bi<sub>2</sub>O<sub>2</sub>CO<sub>3</sub>) are shown in following **Fig. 12**. As shown in **Fig. 12**, the intensity of the photocurrent follows the order of Au NRs (~30 nm)- $\alpha$ -Bi<sub>2</sub>O<sub>3</sub>/Bi<sub>2</sub>O<sub>2</sub>CO<sub>3</sub> >  $\alpha$ -Bi<sub>2</sub>O<sub>3</sub>/Bi<sub>2</sub>O<sub>2</sub>CO<sub>3</sub> > Bi<sub>2</sub>O<sub>2</sub>CO<sub>3</sub> >  $\alpha$ -Bi<sub>2</sub>O<sub>3</sub>. Au NRs (~30 nm)- $\alpha$ -Bi<sub>2</sub>O<sub>3</sub>/Bi<sub>2</sub>O<sub>2</sub>CO<sub>3</sub> shows the strongest photocurrent. According to the literatures, the higher the optical response signal, the higher the separation efficiency of the photo generated electron hole pairs [56]. The photocurrent measurement results demonstrated that the loading of Au NRs largely facilitate the charge carriers separation and transfer, which is consistent with the photocatalytic performance.

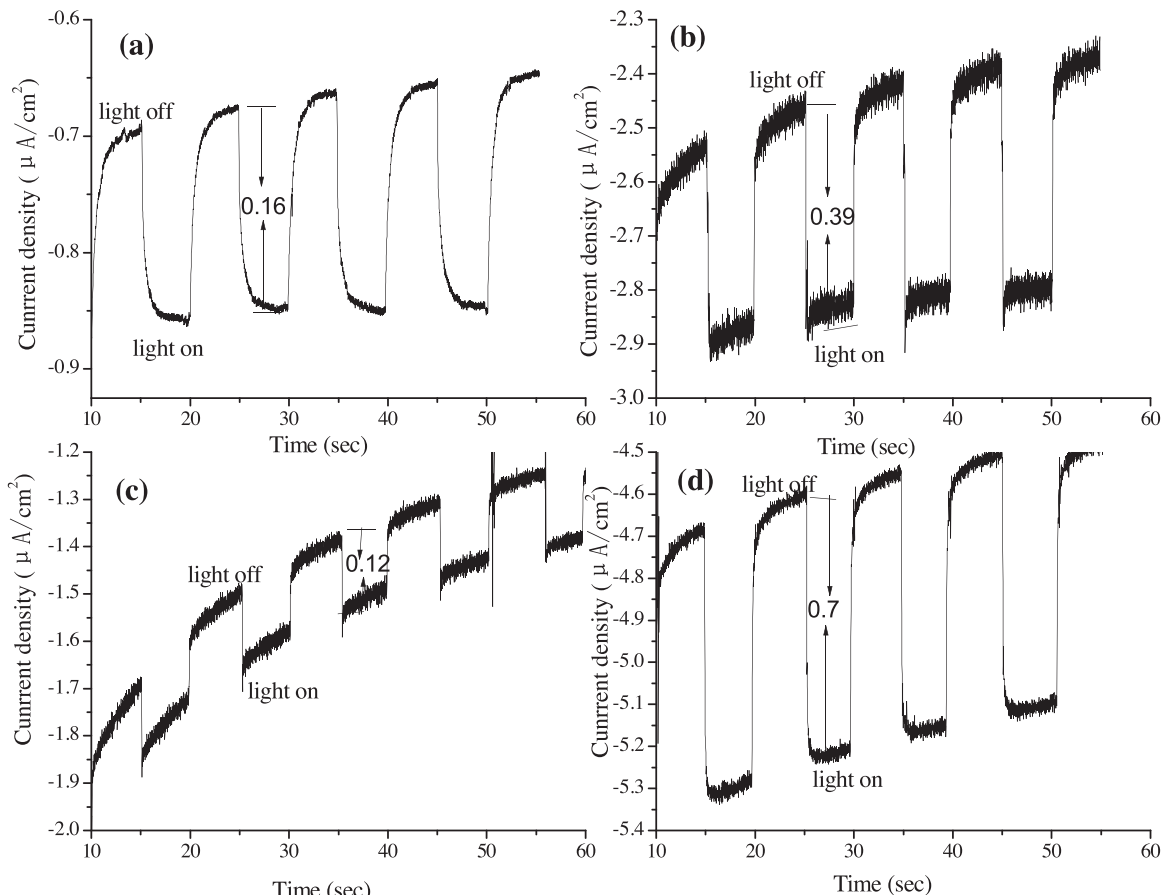


**Fig. 12.** The produced photocurrent density under simulative solar light irradiation (Xenon lamp) for different samples. (a) Bi<sub>2</sub>O<sub>2</sub>CO<sub>3</sub> (b)  $\alpha$ -Bi<sub>2</sub>O<sub>3</sub>/Bi<sub>2</sub>O<sub>2</sub>CO<sub>3</sub>; (c)  $\alpha$ -Bi<sub>2</sub>O<sub>3</sub>; (d) Au NRs (~30 nm)- $\alpha$ -Bi<sub>2</sub>O<sub>3</sub>/Bi<sub>2</sub>O<sub>2</sub>CO<sub>3</sub>.

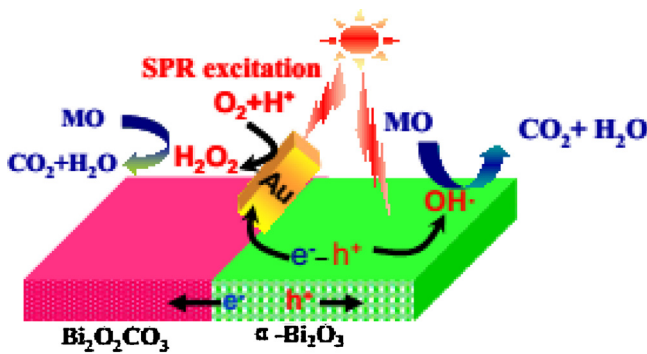


**Fig. 13.** Schematic photocatalytic reaction process and charge transfer of the Au NRs/α-Bi<sub>2</sub>O<sub>3</sub>/Bi<sub>2</sub>O<sub>2</sub>CO<sub>3</sub> heterostructured catalyst under visible-light irradiation. Nanorods: NRs.

Based on the above results, we proposed the following possible reasons to explain the significantly enhanced photocatalytic activity of the α-Bi<sub>2</sub>O<sub>3</sub>/Bi<sub>2</sub>O<sub>2</sub>CO<sub>3</sub> heterostructure and Au/α-Bi<sub>2</sub>O<sub>3</sub>/Bi<sub>2</sub>O<sub>2</sub>CO<sub>3</sub> photocatalyst. In α-Bi<sub>2</sub>O<sub>3</sub>/Bi<sub>2</sub>O<sub>2</sub>CO<sub>3</sub> heterostructure, the potential of the CB: 0.11 eV of α-Bi<sub>2</sub>O<sub>3</sub> is slightly more negative than that of Bi<sub>2</sub>O<sub>2</sub>CO<sub>3</sub> (CB: 0.26 eV) (as shown in Supplementary data Fig. S3). Therefore, the photogenerated electrons in the α-Bi<sub>2</sub>O<sub>3</sub> layer can be transferred to the CB of the Bi<sub>2</sub>O<sub>2</sub>CO<sub>3</sub>, leaving the holes on the BV of α-Bi<sub>2</sub>O<sub>3</sub>. The good interface charge transfer process, as indicated in Fig. 13, promotes the effective separation of photoexcited electrons and holes, and hence decreases the probability of electron–hole recombination, enhancing the photocatalytic activity of α-Bi<sub>2</sub>O<sub>3</sub>/Bi<sub>2</sub>O<sub>2</sub>CO<sub>3</sub> heterostructure.

Over Au/α-Bi<sub>2</sub>O<sub>3</sub>/Bi<sub>2</sub>O<sub>2</sub>CO<sub>3</sub> systems, three reasons could contribute their high photocatalytic efficiency. The first one is that the interface charge transfer process between α-Bi<sub>2</sub>O<sub>3</sub> and Bi<sub>2</sub>O<sub>2</sub>CO<sub>3</sub> also plays the role. But, two more important reasons are the role of the loaded Au NPs. First, the integrated plasmonic Au NSs or NRs on α-Bi<sub>2</sub>O<sub>3</sub>/Bi<sub>2</sub>O<sub>2</sub>CO<sub>3</sub> surfaces may act as electron sinks to retard the recombination of the photogenerated electrons and holes in α-Bi<sub>2</sub>O<sub>3</sub> so as to improve the charge separation on its surfaces. It is known that the Fermi level of gold is 0.5 V (vs NHE) [57], which is more positive than the CB edge of α-Bi<sub>2</sub>O<sub>3</sub> (0.11 eV). At the Au-α-Bi<sub>2</sub>O<sub>3</sub> heterojunction, photogenerated electrons in the α-Bi<sub>2</sub>O<sub>3</sub> could fast transfer to Au particles. The accumulated electrons on Au could reduce the surface O<sub>2</sub> to form H<sub>2</sub>O<sub>2</sub> because the CB level of α-Bi<sub>2</sub>O<sub>3</sub> (0.11 eV vs NHE) is more positive than that of the reaction (1): O<sub>2</sub> + e<sup>-</sup> → O<sub>2</sub><sup>•-</sup> (0.33 V vs NHE), but more negative than that (+0.695 V vs NHE) of reaction (2): e<sub>CB</sub><sup>-</sup> + O<sub>2</sub> + H<sup>+</sup> → H<sub>2</sub>O<sub>2</sub>. The produced H<sub>2</sub>O<sub>2</sub> can be further reduced to •OH radicals as reaction (3): e<sub>CB</sub><sup>-</sup> + H<sub>2</sub>O<sub>2</sub> → •OH + OH<sup>-</sup>. This speculation was supported by the direct evidence of the in situ photoproduction of H<sub>2</sub>O<sub>2</sub> in the visible light irradiated suspension of the pure α-Bi<sub>2</sub>O<sub>3</sub> and Au/α-Bi<sub>2</sub>O<sub>3</sub> [54]. Second, the SPR of gold NPs attached on α-Bi<sub>2</sub>O<sub>3</sub>/Bi<sub>2</sub>O<sub>2</sub>CO<sub>3</sub> surfaces could enhance visible light absorption and photocatalytic efficiency. It has been extensively demonstrated that the plasmon-exciton coupling can result in significant enhancement of charge separation [58]. According to Warren and Thimsen [24], under visible-light irradiation, large gold NPs (>30 nm) in Au/TiO<sub>2</sub> could induce plasmonic near-fields by strong localized-surface-plasmon-resonance (LSPR). The plasmonic near-fields are localized close to the Au-TiO<sub>2</sub> interface. The strong localization of plasmonic near-fields could enhance optical absorption and generate electron–hole pairs for photocatalysis via optical transitions between the localized electronic states in the band gap of the TiO<sub>2</sub>. In our case, the average sizes of Au NSs and Au NRs are close to 30 nm. Therefore, LSPR could take place in Au-α-Bi<sub>2</sub>O<sub>3</sub>/Bi<sub>2</sub>O<sub>2</sub>CO<sub>3</sub> interface, which further enhances the photocatalytic performance. The difference in the shape and structural anisotropy of NSs and Au NRs caused

the different SPR, such as plasmonic resonance absorption wavelength, the intensity of LSPR. Activity test showed that effects of Au NPs on promoting the activity follow the order: Au NSs (~30 nm, 0.0410 min<sup>-1</sup>) < Au NRs (~20 nm, 0.0562 min<sup>-1</sup>) < Au NRs (~35 nm, 0.0520 min<sup>-1</sup>) < Au NRs (~30 nm, 0.0940 min<sup>-1</sup>). It sees that plasmonic Au NPs with moderate aspect ratio, such as Au NRs (~30 nm, aspect ratio: 2) gives the largest ability to increase visible photocatalytic activity, which could be related to its suitable plasmonic resonance absorption wavelength and strong LSPR. •OH production tests confirmed that more •OH radicals were generated by Au NRs (~30 nm)/α-Bi<sub>2</sub>O<sub>3</sub>/Bi<sub>2</sub>O<sub>2</sub>CO<sub>3</sub> under the same photocatalytic condition, which suggests its high capacity to inhibit electron–hole recombination to a large extent.

#### 4 Conclusions

In summary, dendritic-like α-Bi<sub>2</sub>O<sub>3</sub>/Bi<sub>2</sub>O<sub>2</sub>CO<sub>3</sub> heterostructures have been first successfully prepared by using a phase transformation strategy. Then, plasmonic Au NPs including Au NSs (~30 nm) and Au NRs (~20, ~30, and ~35 nm), were loaded onto the α-Bi<sub>2</sub>O<sub>3</sub>/Bi<sub>2</sub>O<sub>2</sub>CO<sub>3</sub> heterostructures. The α-Bi<sub>2</sub>O<sub>3</sub>/Bi<sub>2</sub>O<sub>2</sub>CO<sub>3</sub> and Au-α-Bi<sub>2</sub>O<sub>3</sub>/Bi<sub>2</sub>O<sub>2</sub>CO<sub>3</sub> heterostructured photocatalysts exhibit highly efficient visible-light-driven photocatalytic activities for dye degradation compared to pure α-Bi<sub>2</sub>O<sub>3</sub> and α-Bi<sub>2</sub>O<sub>3</sub>/Bi<sub>2</sub>O<sub>2</sub>CO<sub>3</sub>. As for the α-Bi<sub>2</sub>O<sub>3</sub>/Bi<sub>2</sub>O<sub>2</sub>CO<sub>3</sub> heterostructures, the improved photocatalytic efficiency is attributed to the enhanced charge separation by interfacial charge transfer. Moreover, the loading of Au NSs or Au NRs gives rise to 4 or 5–11 times increase in activity compared to α-Bi<sub>2</sub>O<sub>3</sub>/Bi<sub>2</sub>O<sub>2</sub>CO<sub>3</sub> heterostructures. The effects of Au NPs on promoting the activity follow the increasing order of Au NSs (30 nm) < Au NRs (20 nm) < Au NRs (35 nm) < Au NRs (30 nm). The presence of Au NSs or Au NRs greatly promote the •OH radical production, which is attributed to the significant enhancement of charge separation. Furthermore, the SPR absorption of these large Au NPs on the α-Bi<sub>2</sub>O<sub>3</sub>/Bi<sub>2</sub>O<sub>2</sub>CO<sub>3</sub> nanostructures could have significant contribution to the visible light photocatalytic activities due to their strong plasmonic near-fields. The strategy of the heterostructure synthesis involving Au NPs on the semiconductor inter-surface may have considerable impact on the future development of highly efficient visible light photocatalysts. This work also provides insight on the mechanism behind efficient visible-light plasmonic photocatalysis.

#### Acknowledgments

C.Y. acknowledges the scholarship support from the China Scholarship Council (No. 2011 836054). This work is financially supported by the National Natural Science Foundation of China (Nos. 21567008, 21263005), the U.S. Department of Energy–Office of Basic Energy Sciences (No. DE-FG02-12ER16354), the Young scientists cultivating object program of Jiangxi Province (No. 20122BCB23015), the Young Science and Technology Project of Jiangxi Province Natural Science Foundation (No. 20133BAB21003), The Landing Project of Science and Technology of Colleges and Universities in Jiangxi Province (No. KJLD14046).

#### Appendix A. Supplementary data

Supplementary data associated with this article can be found, in the online version, at <http://dx.doi.org/10.1016/j.apcatb.2015.11.026>.

#### References

- [1] H. Xu, P. Reunchan, S.X. Ouyang, H. Tong, N. Umezawa, T. Kako, J.H. Ye, *Chem. Mater.* 25 (2013) 405–411.

[2] Q.J. Xiang, J.G. Yu, *J. Phys. Chem. Lett.* 4 (2013) 753–759.

[3] A. Kubacka, M. Fernández-García, G. Colón, *Chem. Rev.* 112 (2012) 1555–1614.

[4] C.L. Yu, Q.Z. Fan, Y. Xie, J.C. Chen, Q. Shu, J.C. Yu, *J. Hazard. Mater.* 237/238 (2012) 38–45.

[5] W.Q. Zhou, C.L. Yu, Q.Z. Fan, L.F. Wei, J.C. Chen, J.C. Yu, *Chin. J. Catal.* 34 (2013) 1250–1255.

[6] K. Iwashina, A. Iwase, Y.H. Ng, R. Amal, A. Kudo, *J. Am. Chem. Soc.* 137 (2015) 604–607.

[7] P.Y. Kuang, Y.Z. Su, K. Xiao, Z.Q. Liu, N. Li, H.J. Wang, J. Zhang, *ACS Appl. Mater. Interfaces* (2015), <http://dx.doi.org/10.1021/acsami.5b03527>.

[8] C.L. Yu, G. Li, S. Kumar, K. Yang, R.C. Jin, *Adv. Mater.* 26 (2014) 892–898.

[9] G.S. Li, B. Jiang, X. Li, Z.C. Lian, S.N. Xiao, J. Zhu, D.Q. Zhang, H.X. Li, *ACS Appl. Mater. Interfaces* 5 (2013) 7190–7197.

[10] S.N. Xiao, P.J. Liu, W. Zhu, G.S. Li, D.Q. Zhang, H.X. Li, *Nano Lett.* 15 (2015) 4853–4858.

[11] F. Lin, D. Wang, Z. Jiang, Y. Ma, J. Li, R. Li, C. Li, *Energy Environ. Sci.* 5 (2012) 6400–6406.

[12] B.J. Ma, J.H. Yang, H.X. Han, J.T. Wang, X.H. Zhang, C. Li, *J. Phys. Chem. C* 114 (2010) 12818–12822.

[13] H. Yan, J. Yang, G. Ma, G. Wu, X. Zong, Z. Lei, J. Shi, C. Li, *J. Catal.* 266 (2009) 165–168.

[14] J.H. Yang, D. Wang, H.X. Han, C. Li, *Acc. Chem. Res.* 46 (2013) 2355–2364.

[15] C.L. Yu, K. Yang, Y. Xie, Q.Z. Fan, J.C. Yu, Q. Shu, C.Y. Wang, *Nanoscale* 5 (2013) 2142–2151.

[16] R. Su, R. Tiruvalam, Q. He, N. Dimitratos, L. Kesavan, C. Hammond, J.A. Lopez-Sánchez, R. Bechstein, C.J. Kiely, G.J. Hutchings, F. Besenbacher, *ACS Nano* 6 (2012) 6284–6292.

[17] D. Shiraishi, Y. Tsukamoto, A. Sugano, S. Shiro, S. Ichikawa, T. Tanaka, *ACS Catal.* 2 (2012) 1984–1992.

[18] X.M. Zhou, G. Liu, J.G. Yu, W.H. Fan, *J. Mater. Chem.* 22 (2012) 21337–21354.

[19] M.A. Mahmoud, W. Qian, M.A. El-Sayed, *Nano Lett.* 11 (2011) 3285–3289.

[20] Y. Tian, T. Tatsuma, *J. Am. Chem. Soc.* 127 (2005) 7632–7637.

[21] S. Mubeen, G. Hernandez-Sosa, D. Moses, J. Lee, M. Moskovits, *Nano Lett.* 11 (2011) 5548–5552.

[22] Y. Tian, T. Tatsuma, *J. Am. Chem. Soc.* 127 (2005) 7632–7637.

[23] W.B. Hou, W.H. Hung, P. Pavaskar, A. Goeppert, M. Aykol, S.B. Cronin, *ACS Catal.* 1 (2011) 929–936.

[24] S.C. Warren, E. Thimsen, *Energy Environ. Sci.* 5 (2012) 5133–5146.

[25] A. Tanaka, K. Hashimoto, B. Ohtani, H. Kominami, *Chem. Commun.* 49 (2013) 3419–3421.

[26] Z.H. Zhang, L.B. Zhang, M.N. Hedhili, H.N. Zhang, P. Wang, *Nano Lett.* 13 (2013) 14–20.

[27] Z.W. Liu, W.B. Hou, P. Pavaskar, M. Aykol, S.B. Cronin, *Nano Lett.* 11 (2011) 1111–1116.

[28] M.D.L.R. Peralta, U. Pal, R.S. Zeferino, *ACS Appl. Mater. Interfaces* 4 (2012) 4807–4816.

[29] N. Wang, T. Tachikawa, T. Majima, *Chem. Sci.* 2 (2011) 891–900.

[30] I. Bannat, K. Wessels, T. Oekermann, J. Rathousky, D. Bahnemann, M. Wark, *Chem. Mater.* 21 (2009) 1645–1653.

[31] S.T. Kochuveedu, D.P. Kim, D.H. Kim, *Phys. Chem. C* 116 (2012) 2500–2506.

[32] A. Tanaka, S. Sakaguchi, K. Hashimoto, H. Kominami, *ACS Catal.* 3 (2013) 79–85.

[33] S.K. Cushing, J.T. Li, F. Meng, T.R. Senty, S. Suri, M.J. Zhi, M. Li, A.D. Bristow, N.Q. Wu, *J. Am. Chem. Soc.* 134 (2012) 15033–15041.

[34] H.J. Chen, L. Shao, Q. Li, J.F. Wang, *Chem. Soc. Rev.* 42 (2013) 2679–2724.

[35] V. Subramanian, E.E. Wolf, P.V. Kamat, *J. Am. Chem. Soc.* 126 (2004) 4943–4950.

[36] Z.W. She, S. Liu, M. Low, S.Y. Zhang, Z. Liu, A. Mlayah, M.Y. Han, *Adv. Mater.* 24 (2012) 2310–2314.

[37] Y. Liu, L.F. Chen, J.C. Hu, J.L. Li, R. Richards, *J. Phys. Chem. C* 114 (2010) 1641–1645.

[38] M. Murdoch, G.I.N. Waterhouse, M.A. Nadeem, J.B. Metson, M.A. Keane, R.F. Howe, J. Llorca, H. Idriss, *Nat. Chem.* 3 (2011) 489–492.

[39] Y. Tsukamoto, Y. Shiraishi, S. Sugano, S. Ichikawa, T. Tanaka, *J. Am. Chem. Soc.* 134 (2012) 6309–6315.

[40] X. Zong, H.J. Yan, G.P. Wu, G.J. Ma, F.Y. Wen, L. Wang, C. Li, *J. Am. Chem. Soc.* 130 (2008) 7176–7177.

[41] J. Zhang, Q. Xu, Z.C. Feng, M.J. Li, C. Li, *Angew. Chem. Int. Ed.* 47 (2008) 1766–1769.

[42] N. Garg, C. Scholl, A. Mohanty, R.C. Jin, *Langmuir* 26 (2010) 10271–10276.

[43] P. Madhusudan, J. Zhang, B. Cheng, G. Liu, *CrystEngComm* 15 (2013) 231–240.

[44] F. Dong, A.M. Zheng, Y.J. Sun, M. Fu, B.Q. Jiang, W.K. Ho, S.C. Lee, Z.B. Wu, *CrystEngComm* 14 (2012) 3534–3544.

[45] K. Fukami, S. Nakanishi, H. Yamasaki, T. Tada, K. Sonoda, N. Kamikawa, N. Tsuji, H. Sakaguchi, Y. Nakato, *J. Phys. Chem. C* 111 (2007) 1150–1160.

[46] G.R. Li, C.Z. Yao, X.H. Lu, F.L. Zheng, Z.P. Feng, X.L. Yu, C.Y. Su, Y.X. Tong, *Chem. Mater.* 20 (2008) 3306–3314.

[47] S. Eustis, M. El-Sayed, *J. Phys. Chem. B* 109 (2005) 16350–16356.

[48] J.Z. Bian, S. Zhu, Y. Wang, X. Cao, H. Qian, H. Li, *J. Phys. Chem. C* 112 (2008) 6258–6262.

[49] D.B. Ingram, S. Linic, *J. Am. Chem. Soc.* 133 (2011) 5202–5205.

[50] F. Dong, Y.J. Sun, M. Fu, W.K. Ho, S.C. Lee, Z.B. Wu, *Langmuir* 28 (2012) 766–773.

[51] S. Shamaila, A.K.L. Sajjad, F. Chen, J.L. Zhang, *Appl. Catal. B* 94 (2010) 272–280.

[52] V.S. Dharmadhikari, S.R. Sainkar, S. Badrinarayanan, A. Goswami, *J. Electron Spectrosc. Relat. Phenom.* 25 (1982) 181–186.

[53] W.S. Epling, G.B. Hoflund, J.F. Weaver, S. Tsubota, M. Haruta, *J. Phys. Chem.* 100 (1996) 9929–9934.

[54] H.Y. Jiang, K. Cheng, J. Lin, *Phys. Chem. Chem. Phys.* 14 (2012) 12114–12121.

[55] K. Ishibashi, A. Fujishima, T. Watanabe, K. Hashimoto, *Electrochim. Commun.* 2 (2000) 207–210.

[56] L.Q. Jing, Z.H. Sun, F.L. Yuan, B.Q. Wang, B.F. Xin, H.G. Gu, *Sci. China Chem.* 36 (2006) 53–57.

[57] V. Subramanian, E.E. Wolf, P.V. Kamat, *J. Am. Chem. Soc.* 126 (2004) 4943–4950.

[58] J.L. Wu, F.C. Chen, Y.S. Hsiao, F.C. Chien, P.L. Chen, C.H. Kuo, M.H. Huang, C.S. Hsu, *ACS Nano* 5 (2011) 959–967.